

Research Article

Localization by Acoustic Emission in Transversely Isotropic Slate

Bjorn Debecker¹ and André Vervoort²

¹*K.U.Leuven, Spatial Applications Division Leuven, B3000 Leuven, Belgium*

²*K.U.Leuven, Research Unit Mining, B3000 Leuven, Belgium*

Correspondence should be addressed to Bjorn Debecker, bjorn.debecker@sadl.kuleuven.be

Received 23 December 2010; Accepted 15 May 2011

Academic Editor: Joseph C. S. Lai

Copyright © 2011 B. Debecker and A. Vervoort. This is an open access article distributed under the Creative Commons Attribution License, which permits unrestricted use, distribution, and reproduction in any medium, provided the original work is properly cited.

A method for localization by acoustic emission in transversely isotropic media is developed and validated. Velocities are experimentally measured and then used to calculate a database of theoretical arrival times for a large number of positions. During an actual test, positions are assigned by comparing measured arrival times with the database's arrival times. The method is applied during load tests on slate samples and compared with visual observations of fractures. The localization method allowed for a good identification of the regions of fracturing at different stages during the test.

1. Introduction

Rock mechanical tests traditionally focus on the determination of mechanical parameters, for example, Young's modulus, compressive and tensile strength. The natural origin of rock results in a wider spreading of these parameters than for man-made materials.

In nature, many rock types are found that consist of a layered structure. This can be created by different stages of sediment deposit as in sedimentary rocks or by reorientation of the crystal structure due to high pressure and temperature as for metamorphic rocks. When the subsequent layers or bands are roughly parallel, the rock mechanical properties are typically found to be transversely isotropic. Thus, these properties are dependent on the angle between direction of loading and the direction of layering. For many types of layered rock, this relation is determined experimentally by load tests [1, 2]. However, studies on the fracture process itself in anisotropic rock are less frequent [3, 4]. Knowledge on the initiation and further growth of fractures is, among others, very valuable for the validation of numerical simulations.

During the loading of a sample, visual observations can generally only be made on the outside surfaces of the sample. Such visual recordings can be used for descriptive observations [5, 6] or used as input, for example, strain deformation [7]. While microscopy [8] can provide information on the interior of the sample, it cannot be applied during load

testing. On the other hand, techniques like μ CT have been applied to extract information of the interior samples during loading [8, 9], but this is currently restricted to very small dimensions. Microfractures that develop in rock or in other material generate elastic strain waves that can be recorded by acoustic emission (AE) sensors. By determining the position of origin of these emissions, information is provided on the fracture process in the interior of the sample. This technique is called localization. Though AE measurements have been introduced in mechanical testing for a long time [10–13], the application of AE localization in rock material is still open for extended research.

In this study, AE localization has been performed on transversely isotropic slate during uniaxial loading. Typically, there is a certain margin of error on wave velocity, and thus on localization due to heterogeneity of rock material. For this type of material, the pronounced layered structure of slate and its orientation-dependent velocities introduce an additional degree of difficulty. Localization in anisotropic media has been studied in the field of material sciences, where theoretically sound solutions have been formulated [14–17]. However, these solutions are based on homogeneous materials, with little variation on their material parameters. Aicher et al. [18] studied localization in another natural, heterogeneous material, namely, wood, but they stuck to a 2D localization. Given the natural heterogeneity of rock, in this paper, it was opted for a more empirical approach.

The research is part of a larger study for a better insight in the fracture process in transversely isotropic rock by means of laboratory experiments and numerical simulations [19].

2. Experimental Determination of the Directional Dependent Wave Velocities and Validation

Before localization can be applied, the wave velocities within the tested material have to be determined. The rock material in this study is metamorphic slate from a quarry in Herbeumont, Belgium. The slate is formed by metamorphosis of sedimentary clay deposits and consists almost entirely of quartz, sericite, chlorite, and cubic pyrite inclusions. To be more precise, the rock is actually a phyllite, that is, a gradation in the degree of metamorphism between slate and mica schist. The rock has a fine and homogeneous structure, a very low porosity with a value of 0.016 and a mass density of 2700 kg/m^3 [19, 20]. It consists of many parallel planes defined by the parallel arrangement of the platy mineral crystals. The rock is at its weakest and preferably breaks along these planes, also called the schistosity direction. Laboratory tests [19] have shown that the average UCS value for θ equal to, respectively, 0° and 90° are, respectively, 135.4 MPa and 49.5 MPa. Corresponding values for Young's modulus are, respectively, 19.8 GPa and 40.5 GPa. This illustrates that the slate rock has a distinct anisotropy both in strength and elasticity. Measurements of horizontal deformations were often unreliable given the small values of deformation (smaller than 0.1 mm). Therefore, only for θ equal to 0° a reliable value for Poisson's ratio was calculated at a value of 0.18.

The wave velocity in slate is determined by breaking a pencil tip at a known position, on a straight line between two sensors. The velocity in the direction of this line is calculated as the difference in distance to both sensors divided by the arrival time difference of the signal. The pencil tip breaking is found to be a suitable simulated source of AE by Nielsen [21] and Van de Steen [22]. AE is measured using an AMSY-5 System by Vallen GmbH. Each signal is amplified by a preamplifier with an amplification of 34 dB. Four wide-band sensors are used of type B1025 (Digital Wave Corp., USA), which have a radius of 4.5 mm and a frequency range from 50 kHz to 2 MHz. The minimal threshold to measure signals is set to 27.9 dB (which corresponds to 25 mV). An example of the recorded waveform of such a pencil break is presented in Figure 1(a). The amplitude peak is generally situated between 200 kHz and 400 kHz, and the signal holds no significant information for frequencies above 1000 kHz.

The velocity in slate is first determined in 2D, on the surface of a slate sample in which the schistosity planes are orthogonal to the outer surface. The velocity is calculated for different directions, all within this plane orthogonal to the schistosity. The angle of direction, θ is varied between 0° (parallel to the schistosity) and 90° (orthogonal to the schistosity) on a 10° -interval (Figure 1(b)).

A maximum velocity is measured parallel to the schistosity, $v_{//}$ of $5,593 \text{ mm}/\mu\text{s}$ and a minimum velocity, orthogonal

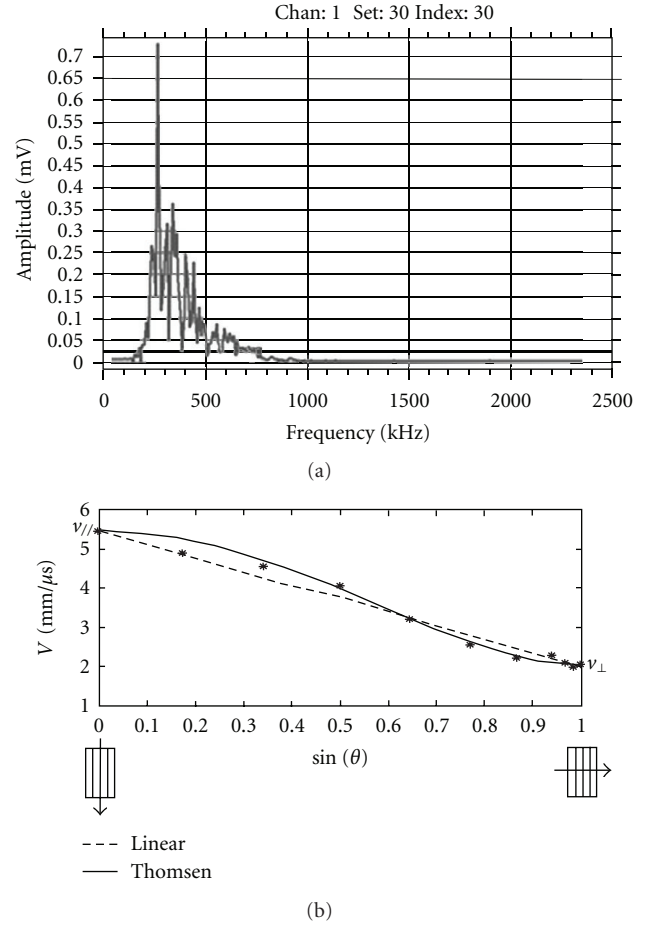


FIGURE 1: (a) Amplitude distribution in the frequency spectrum of a measured hit. The thick horizontal line indicates the threshold level (27.9 dB = 0.025 mV). (b) Slate wave velocity in function of the angle with the schistosity, γ : measured (dots) and linearized (dotted line).

to the schistosity, v_{\perp} of $2,075 \text{ mm}/\mu\text{s}$. In general, the velocity $v(\theta)$ is found to be approximately linear proportional to the sinus of the angle θ between its direction and the schistosity

$$v(\theta) = v_{//} - (v_{//} - v_{\perp}) \cdot \sin(\theta). \quad (1)$$

However, a more physically sound approximation can be found by Thomsen [23], where the anisotropic velocity relation is derived based on the coefficients of the elastic tensor. In this case, the velocity is proportional to the fourth power of the sine (/cosine) of θ

$$v(\theta) = v_{\perp} + (v_{//} - v_{\perp}) \cdot \sin^4\left(\frac{\pi}{2} - \theta\right) + \delta \cdot v_{\perp} \cdot \cos^2(\theta) \cdot \sin^2(\theta), \quad (2)$$

with Thomsen parameter δ equal to -0.05 for the Herbeumont slate.

It can be seen from Figure 1(b) that this last approximation has roughly the same quality as the linear relation from (1).

In 3D, the velocity v is directional dependent in three dimensions. To illustrate this, Figure 2 shows a set of parallel schistosity planes. Assume a local set of axes, $x'y'z'$ where the $x'y'$ -plane is orthogonal to the schistosity plane, and thus the $x'z'$ -plane parallel to the schistosity planes. Any given direction \vec{r} can be uniquely determined by two angles, θ and ψ . If $r_{x'y'}$ is the component of the direction in the plane orthogonal to the schistosity ($x'y'$), then θ is the angle between the $r_{x'y'}$ and the x' -axis, in analogy with the 2D convention. ψ is the angle that \vec{r} makes with the plane orthogonal to the schistosity ($x'y'$), thus the angle between $r_{x'y'}$ and \vec{r} .

First, for any direction within the plane $x'y'$, orthogonal to the schistosity, the velocity $v_{x'y'}(\theta)$ is defined by (1). Second, given the transversal anisotropy, one has observed that parallel to the schistosity plane, the velocity is isotropic, and thus equal to $v_{//}$ in any direction. Thus, if one wants to determine the velocity in an arbitrary direction \vec{r} , first consider the plane defined by the z' -axis and \vec{r} . This $z'r$ -plane makes an angle θ with the x' -axis and within the $z'r$ -plane the velocity varies between $v_{x'y'}(\theta)$ and $v_{//}$.

Similar as for a plane orthogonal the schistosity, the velocity in this plane is linear proportional to $\sin(\psi)$

$$v(\theta, \psi) = v_{x'y'}(\theta) + (v_{//} - v_{x'y'}(\theta)) \cdot \sin(\psi). \quad (3)$$

Filling (1) in (3), with $v_{x'y'}(\theta) = v(\theta)$ results in

$$\begin{aligned} v(\theta, \psi) \\ = [v_{//} - (v_{//} - v_{\perp}) \cdot \sin(\theta)] + (v_{//} - v_{\perp}) \cdot \sin(\theta) \cdot \sin(\psi). \end{aligned} \quad (4)$$

It is obvious in (4) that for any direction parallel to the schistosity planes ($\theta = 0^\circ$), the velocity is maximal, namely, $v_{//}$.

A final note on the experimental determination of the velocity has to be made. In a first attempt, the velocity was derived by transmitting an ultrasonic P-wave on one end of a sample and receiving it on the other end. This was done by a Steinkamp Ultrasonic tester BP7 with a 50 kHz transmitter. However, such a transmitter emits a pulse, and thus, the pulse velocity is measured, which is not the same as the phase velocity in an anisotropic medium. Thus, this results in an underestimation of the velocities, and hence a worse localization.

3. A Model for Position Estimation

The aim of the ongoing research is to monitor the fracture process in slate samples by measuring AE during the uniaxial loading of a rectangular slab of slate. The width (60 mm) and height (130 mm) of the samples are larger than the thickness of the samples (30 mm). As such, it was hoped that a 2D approximation would suffice for this problem. Hence, a straightforward methodology for 2D localization was first developed, followed by a model for 3D localization.

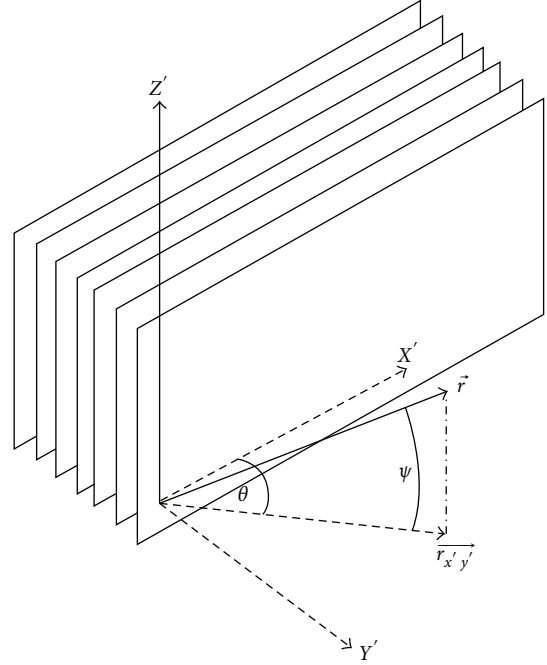


FIGURE 2: Set of schistosity planes ($x'z'$) with local set of axes $x'y'z'$. Each direction r is defined by its angles θ and ψ , respectively, with the y' -axis and with the plane orthogonal to the schistosity, $x'y'$.

The method for localization is relatively straightforward. For each acoustic event recorded by the sensors, from now on called a *hit*, the arrival time difference (ATD) for a pair of two sensors is determined. When considering an isotropic material (i.e., identical velocity in any direction), the isolines for all points with a constant ATD are hyperboles with the sensors as foci. When working with three sensors, the hit can be localized as the point of intersection of the two calculated hyperboles resulting from two different pairs of sensors (Figure 3).

Mathematically, the ATD between sensor 1 and sensor 2 can be described by

$$\begin{aligned} \text{ATD}_{1,2} = \Delta t_{1,2} = t_2 - t_1 &= \frac{\Delta d_{1,2}}{v} \\ &= \frac{\sqrt{(x - x_2)^2 + (y - y_2)^2} - \sqrt{(x - x_1)^2 + (y - y_1)^2}}{v}, \end{aligned} \quad (5)$$

in which (x_1, y_1) is the position of sensor 1, (x_2, y_2) is the position of sensor 2, $\Delta d_{1,2}$ is the difference in distance between event and respectively, both sensors, and v the wave velocity in the material. Similarly, the equation can be derived for $\text{ATD}_{1,3}$, between sensor 1 and a third sensor 3 with position (x_3, y_3) . This results in two equations with two unknowns, namely, x and y . Thus, the 2D position of the hit can be determined. It is true that a third equation, namely, $\text{ATD}_{2,3}$ can be formulated though this third equation is

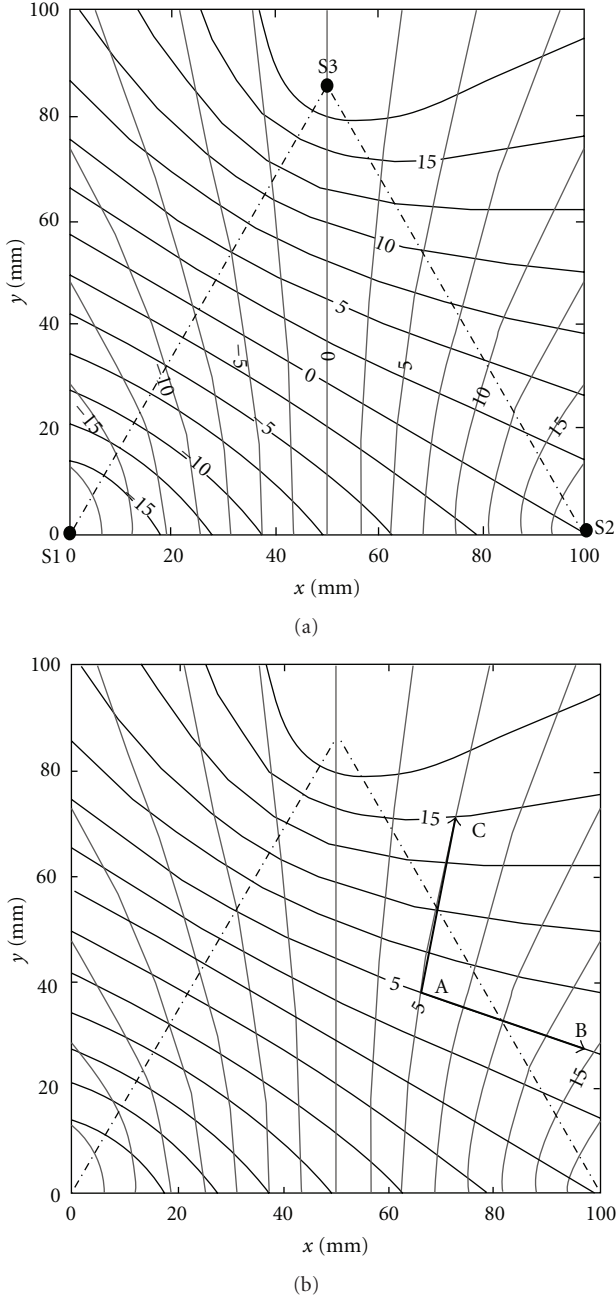


FIGURE 3: Isotropic medium with a velocity of 5 mm/μs. (a) Hyperbolae as isolines of constant arrival time differences (μs) for sensors S1 and S2 (grey), respectively, sensors S1 and S3 (black). (b) ATD increases with increasing distance from the triangle (from A to B or from A to C).

dependent on the other two, and hence, it is not considered here. Low anisotropy is one of the prerequisites for the localization reliability with this method as noted by Lavrov et al. [24].

Figure 3(a) shows a set of hyperbolae or isolines, that is, lines on which the ATD to a given pair of sensor is constant for an equilateral triangular array of 3 sensors.

It should be noted here that for optimal localization, the position of the hit should be situated within the polygonal

defined by the sensors. The reason for this is simple and illustrated in Figure 3(b). If one moves out of the triangle defined by the three sensors, at least one of the two ATDs is increasing in absolute value. In this example, if one stays on a isoline for S1–S3 but moves away from the triangle (from point A to point B), $ATD_{1,3}$ increases. In the same way, $ATD_{1,2}$ increases if one moves out of the triangle on a S1–S2 isoline (from point A to point C). Now, (4) demonstrates that the calculated distance differences Δd are linear proportional to the measured ATD. This implies that any inaccuracy on the applied velocity has an increasing effect on the inaccuracy of the calculated position, with increasing distances from the sensors. Thus, the farther away points are situated from the centre of the sensor grid, the larger the localization error.

Labuz et al. [25] calculated error contours of position estimates for a 10% variation in measured velocity. In order to reduce position errors more sensors can be added, and the position can be found by minimizing the set of over determined equations that follows from (4) in this case.

When the material is anisotropic, the localization becomes more complicated. The wave velocity v_i is now dependent on the direction θ_i . Therefore, (5) is now adapted to

$$\begin{aligned} ATD_{1,2} = \Delta t_{1,2} &= t_2 - t_1 = \frac{d_2}{v_2} - \frac{d_1}{v_1} \\ &= \frac{\sqrt{(x - x_2)^2 + (y - y_2)^2}}{v_2} - \frac{\sqrt{(x - x_1)^2 + (y - y_1)^2}}{v_1}, \end{aligned} \quad (6)$$

with d_i the distance to sensor i and v_i the wave velocity in the direction with a coefficient of direction

$$\tan(\theta_i) = \frac{(y - y_i)}{(x - x_i)}. \quad (7)$$

The isolines now become “distorted” hyperbolae. If the wave velocity is known as a function of direction, $v_i(\theta_i)$, one has a set of 5 equations ((6) for sensors 1-2 and for sensors 1-3, and $v_1(\theta_1)$, $v_2(\theta_2)$, $v_3(\theta_3)$ according to (1) for 5 unknowns (x , y , v_1 , v_2 , v_3). However this is a set of implicit equations, and a more advanced technique is required to solve them.

Theoretically, given an array of sensors with known wave velocities in each direction, the ATD to each pair of sensors can be calculated for every position on a reference grid. Thus, a database of theoretical arrival times for all these positions can be constructed. Then, when a hit is recorded during testing, its position can be estimated by comparing the measured ATDs with the calculated ATDs from the reference grid database. The comparison is done by minimizing the error on ATD. Thus, the reference grid point $(x_n^{\text{ref}}, y_n^{\text{ref}})$ that has the least sum of square differences between its ATDs and the set of measured ATDs, Ω is determined as the origin of the hit $\alpha(x_\alpha, y_\alpha)$

$$\Omega = \min \left(\sum_{\substack{i=1-4 \\ j=i+1-4}} \left[ATD_{i,j}^{\text{ref}}(x_n^{\text{ref}}, y_n^{\text{ref}}) - ATD_{i,j}(x_\alpha, y_\alpha) \right]^2 \right). \quad (8)$$

It should be noted that for 4 sensors, all 6 ATDs are used in this calculation. The smaller Ω , the more efficient the position could be assigned.

Some remarks on this methodology should be formulated. First, it is important that velocities are well known. Since the velocity is assumed to be known exactly and to be the same in each direction, small errors in actual velocity lead to errors on the estimated position. By assigning the position for which the sum of square errors is minimal, this position error is only partially reduced. The magnitude of Ω can, therefore, be an indication of the uncertainty on the estimated position.

Second, each hit that is recorded by all sensors, is localized. Even when the hit comes from outside the grid, it is simply assigned to the position where Ω is minimal. This results in a position on one of the edges of the grid. To overcome such inaccurate estimations, a maximum value for Ω can be set, above which localization is left out.

Note that alternative criteria can be formulated based on the approximation errors [26].

4. Validation of the Model in 2D

Validation is performed by inducing hits on well-known positions by breaking a pencil tip and comparing the actual positions with the calculated positions. Four sensors are placed on the corners of a 40 mm × 100 mm array, centrally positioned on a 60 mm × 115 mm slate sample (Figure 4). Thus, the sample has the same dimensions as the slabs from the load tests that are performed at a later stage, only a bit shorter (115 mm instead of 130 mm). The schistosity is parallel to the longest edge of the sample. A regular grid is drawn with the sensors on the corners and with a distance between two neighbouring gridlines of 10 mm, both in vertical and horizontal direction. Hits are induced on all grid points that lie within the array of sensors. Figure 5 illustrates the real position of each hit (except for the hits on the boundaries of the array) together with an arrow pointing towards its localized position.

Figure 6(a) shows the histogram of the allocation efficiency Ω for all points. It can be seen that for the majority of points (43 out of a total of 51) Ω is smaller than or equal to $50 \mu\text{s}$. However, if the distinction is made between points lying on the edge of the grid (grey bars) and points in the interior (white bars), it is clear that all points with $\Omega > 50 \mu\text{s}$ are edge points. Thus, localization of edge points is less reliable. This is in agreement with earlier observations by de Barquin and Nicaise [20]. They reported that the farther away points are situated from the centre of the sensor grid, the larger the localization error. Based on the information of the histogram, it is decided to set Ω_{max} at a value of $50 \mu\text{s}$, for this configuration. From here on, the focus is on the interior points. Figure 6(b) shows the histogram of Ω , only for the interior points but with smaller class widths. Most interior points are localized with Ω smaller than $5 \mu\text{s}$. Figure 6(c) presents the distribution of the localization error of the interior points, that is, the distance between the position by localization and the real position. The average position error

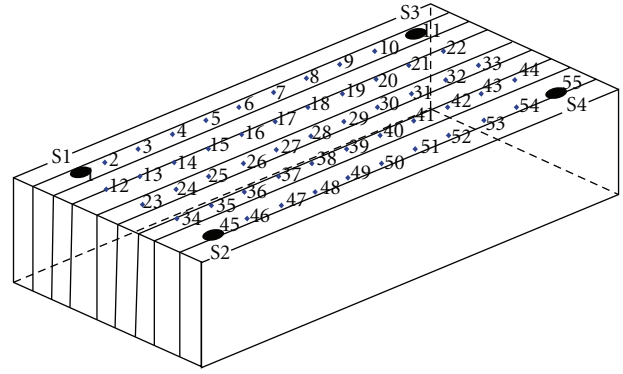


FIGURE 4: Slate sample with dimensions 60 mm × 115 mm × 30 mm. Positions of the test grid (40 mm × 100 mm) on the front side of the sample, with the sensors (S1–S4) in the same plane. Schistosity is indicated by the thin lines.

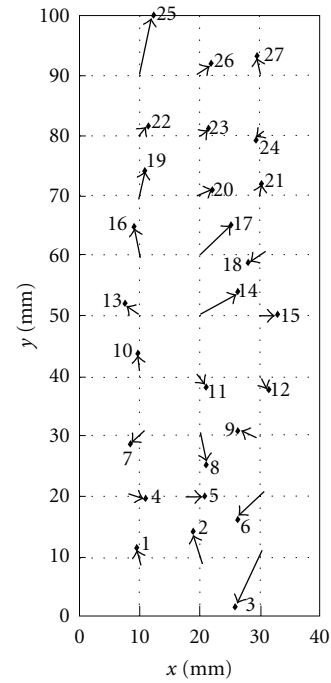


FIGURE 5: Positions within a reference grid (40 mm × 100 mm). Arrows point from the exact position to the location calculated by localization. Schistosity is parallel to the y-axis. One sensor is located at each corner of this grid.

is 3.7 mm and 74% of the points are localized with an error smaller than 4.5 mm (which corresponds to the radius of the applied sensors). Note that the average error of 3.7 mm is an order of magnitude larger than the interlayer distance of the reference grid (0.1 mm). Thus, it would be useless to apply a reference grid with an even smaller interlayer distance.

Finally, Figure 7 shows the scatter plot of Ω versus the localization error for the interior points only. Here it is clear that for increasing values of Ω , the localization error increases, and thus, the localization is less reliable (I on Figure 8). On the other hand, for small values of Ω (smaller than $10 \mu\text{s}$), there is no correlation with the localization error

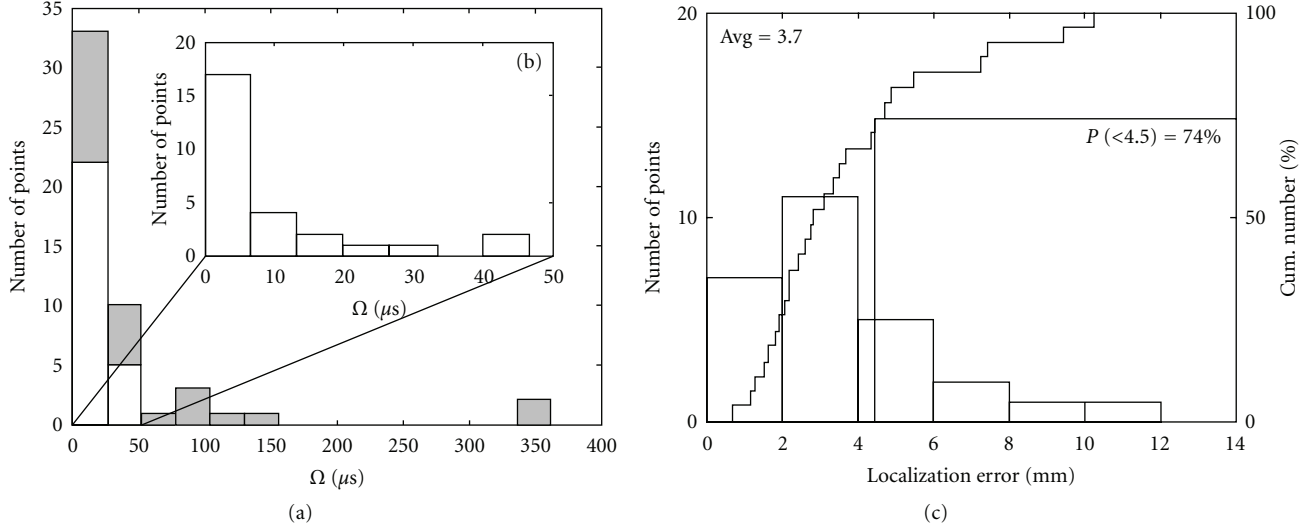


FIGURE 6: (a) Histogram of allocation efficiency Ω for all points: interior points (white) and edge points (grey). (b) Histogram of Ω for interior points only. (c) Histogram of localization error (left axis) and cumulative distribution (right axis) for interior points only.

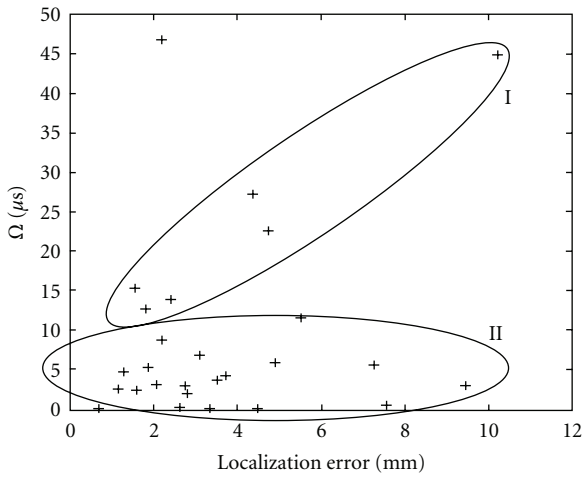


FIGURE 7: Scatter plot of the localization error versus the allocation efficiency Ω for the interior points only. Increasing displacement error for increasing Ω (I) while for small values of Ω ($<10 \mu\text{s}$), there is no correlation with the displacement error (II).

(II on Figure 7). An inaccurate position can be allocated with a very small value for Ω when the ATDs of this (inaccurate) position satisfy (6) nearly exactly for each pair of sensors. When (6) is satisfied less well, Ω increases and becomes linear dependent to the localization error.

As said earlier, the original study intended to be two dimensional. This is because the authors are mainly interested in the position of events within the plane formed by the two largest dimensions. However, during a load test, hits can be generated on both outer surfaces but mainly within the sample. In order to verify if the third dimension can be neglected, a new sensor configuration is chosen. To test the most extreme case, the sensors are attached to the other side of the sample as where the pencil is broken. Thus, all hits are

generated by pencil tip breaking, in one plane on a $40 \text{ mm} \times 100 \text{ mm}$ grid, while the 4 sensors are lying on the corners of the grid, but in a parallel plane at a distance of 30 mm. The 2D-localization generates bad results for this configuration. The average displacement error by localization is 6.4 mm, which is around 70% more than in the configuration where the hits are induced in the plane of the sensors. Therefore, the localization method is extended into 3D.

In 3D, the methodology is similar though now (5) becomes

$$\begin{aligned} \text{ATD}_{1,2} &= \Delta t_{1,2} \\ &= \frac{\sqrt{(x-x_2)^2 + (y-y_2)^2 + (z-z_2)^2}}{v_2} \\ &\quad - \frac{\sqrt{(x-x_1)^2 + (y-y_1)^2 + (z-z_1)^2}}{v_1}, \end{aligned} \quad (9)$$

while (8) is extended to

$$\Omega = \min \left(\sum_{\substack{i=1 \rightarrow 4 \\ j=i+1 \rightarrow 4}} \left[\text{ATD}_{i,j}(x_n^{\text{ref}}, y_n^{\text{ref}}, z_n^{\text{ref}}) - \text{ATD}_{i,j}(x_\alpha, y_\alpha, z_\alpha) \right]^2 \right). \quad (10)$$

5. Application during a Uniaxial Load Test

An experimental setup is made in an attempt to correlate data from AE localization with visual observations during the loading of a sample. Five rectangular samples (B01–B05) are tested with a width and a height of, respectively, 60 mm and 130 mm. The thickness of the samples is 30 mm. The samples are loaded as indicated by the arrows in Figure 8(a). The schistosity makes an angle of 20° with the bottom (horizontal) surface, while the angle with the front surface

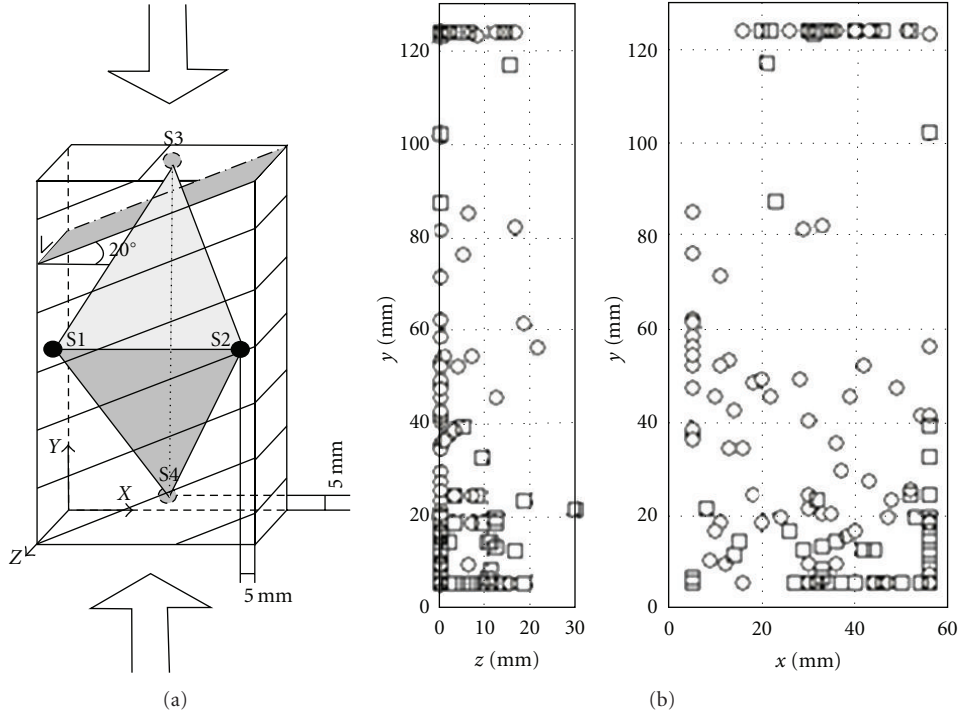


FIGURE 8: (a) Sensor configuration (S1 to S4) for a uniaxial compressive test on a slate sample. The parallel lines represent the orientation of schistosity (20°). Each centre of a sensor is positioned at 5 mm of the nearest edge. (b) Slate sample B02. Positions calculated by 3D localization within the zy -plane (left) and the xy -plane (right). Circles and squares point out prepeak, respectively, postpeak hits.

is 90° ($\pm 2^\circ$ due to sample preparation accuracy and natural variability). The intention is to study the fractures as 2D features under this configuration.

An absolute minimum of 4 sensors is required for a 3D localization. To allow 2D localization, the minimum of 3 sensors cannot lie on one line. In the same way, for 3D localization, the 4 sensors cannot lie within the same plane. Therefore, in order to have as much volume covered as possible, the configuration on Figure 8(a) is chosen. Two sensors are attached on the front surface, at half the height of the sample, one on the left (S1), and one on the right (S2). They are both positioned at a distance of 5 mm from the nearest edge. Two other sensors are both located on the back of the sample, halfway along the width. Sensor S3 is attached at 5 mm from the top of the sample, while S4 is situated at 5 mm from the bottom of the sample, both on the vertical symmetry axis of the back side. Optimal results for localization are found within the tetrahedron formed by the four sensors (Figure 8(a)). The tetrahedron is the 3D analogy for the 2D triangle configuration as described in Figure 3. The volume of the tetrahedron covers about one third of the total volume of the sample. Thus, if acoustic events occur outside this central array localization, efficiency decreases rapidly. Ideally, another accuracy check should be done with this new sensor array, similar as for the previous setup. However, the rock material is cut from the same block and believed to have the same properties and amount of heterogeneity. In addition, for a decent accuracy check, (synthetic) hits should be generated within the sample, but

this is physically impossible under the current laboratory conditions. Therefore, it is aimed to look for a regional localization rather than an exact one. Future improvements can enhance the results discussed below.

If a sensor configuration is chosen deliberately so that the majority of hits lie outside the array, the configuration is referred to as an *inside-out array* though it is described in literature that one should not opt for this [27].

The 3D velocity can be calculated according to (4), taking into account the 20° inclination of the schistosity relative to the (horizontal) zx -plane

$$v(\theta, \psi) = [v_{//} - (v_{//} - v_{\perp}) \cdot \sin(\theta - 20^\circ)] + (v_{//} - v_{\perp}) \cdot \sin(\theta - 20^\circ) \cdot \sin(\psi), \quad (11)$$

where θ and ψ are orientated towards the xyz -axes as shown in Figure 2, but this time the xyz -axes are orientated within the sample as shown in Figure 8(a).

The sample loading is displacement controlled. All samples are loaded initially at a rate of 0.5 mm/min. At a given load (80 kN for B01, 50 kN for all other samples) the loading rate is decreased to 0.05 mm/min. The following discussion focuses on one sample, B02 as an example. Figure 8(b) shows the acoustic hits for B02 as calculated by 3D localization in the xy -plane (left) and the zy -plane (right). Only the hits that are recorded by all 4 sensors and with a least sum of square differences Ω smaller than $300 \mu\text{s}$ are withheld. The value of $300 \mu\text{s}$ is determined by looking at the histogram of Ω of all localized hits upon which it is decided that

for larger values, the localization is unreliable. The hits are grouped according to their time of appearance. The circles and squares represent hits in, respectively, prepeak and postpeak stage of loading. Most pre-peak hits are found in the backside of the sample, that is, small z -values. Though many of them are localized outside the sensor array, and thus have a decreased quality of localization, this does not explain their asymmetry within the zy -plane. As they are found before the first visual observations of fracturing, it could be that their origin is rather due to friction (sensor sample or loading platen sample) rather than due to micro cracking.

The postpeak hits are more scattered when projected on the zy -plane though the majority is still in the back half of the sample. During the loading tests, the velocities are regarded as load independent. However, several authors have shown that acoustic velocities are load dependent [28, 29]. The general theory is that in the first part of a loading test velocities increase due to closure of preexisting fractures (or also schistosity in this case). As microcracking starts later in the test, velocities start to decrease again, already before the load peak is reached. Both authors determined these velocity increments in the order of magnitude of 10%. In Figure 9, the influence of the calculated positions for a velocity increase (Figure 9(b)) as well as decrease (Figure 9(c)) of 10% is shown. It is observed that especially a decrease of v_{\perp} and v_{\parallel} positions the hits towards higher z -values (more to the front), and thus more evenly distributed over the thickness. Since a decrease in velocity is to be expected in the postpeak stage, this would thus reposition the postpeak hits more evenly distributed. Within the plane of the largest dimensions (xy -plane), the projections of the hits are more spread. The locations within this plane are compared with video images of the front of the sample during testing that are summarized schematically in drawings. The occurrence of separate fractures is then also situated on the load-time graph of each test as shown in Figure 10 by the consequent numbers. The load peak is situated at “3” on this curve. In addition, Figure 10 shows the cumulative number of localized hits in function of time. For B02, there are 180 hits. All other samples have a similar number of total hits, except for one sample, B05 that has only very few hits in the post-peak region (15), and thus contains little information during that stage.

Finally, this combined information is used to correlate with the AE-localization data. Figure 11 presents the different stages of fracture growth that are visually observed, referred to by the same numbers, together with the positions of the localized acoustic events, for sample B02.

Most AE-activity is observed in the prepeak stage, and these hits are located all over the sample (“before 3” in Figure 11). They are probably due to the closing of schistosity layers and in a later stage to the occurrence of microcracks that are not yet visible by the naked eye. Larger concentrations of localized hits near the contact edges of the sample are most likely due to displacement and/or deformation at the sample-loading piston contact.

In the postpeak stage, starting with fracture 4b, the hits are localized in the same zone as the visual observations of the fracture (i.e., 4b: upper zone, 6: lower zone, 7-8: upper zone, 9-10: lower zone, and 11-10: lower zone). Once

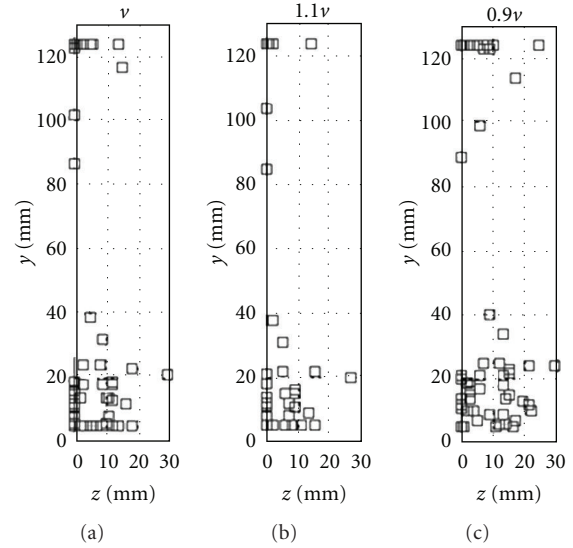


FIGURE 9: Slate sample B02. Positions calculated by 3D localization within the zy -plane for the original velocities (a) and for, respectively, an increase (b) and decrease (c) in velocities by 10% (right).

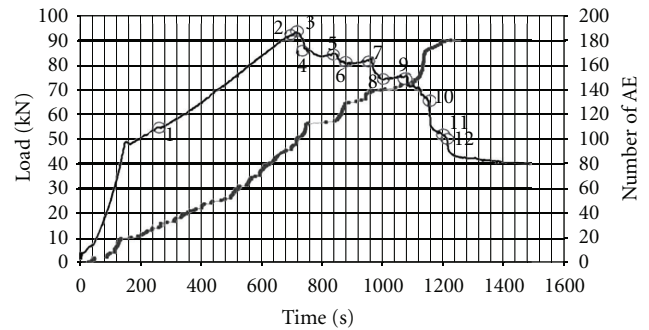


FIGURE 10: Slate sample B02. Load versus time (left axis) and cumulative number of AE hits versus time (right axis). The circles correspond to the observations of fractures.

fractures are formed, they are important hindrances for acoustic emissions from other locations to reach the sensors. Opening of fractures can induce considerable damping, and, in addition, the anisotropic nature of the velocity as described by (11) is affected. This explains the decreased amount of localized hits in the prepeak stage. The accuracy of the localized positions is too small to pinpoint the exact position of hits along specific fractures. However, often there is a quite good correspondence between the zone where fractures are occurring and the zone where AE hits are localized.

6. Conclusion

An algorithm is developed to localize acoustic events in a transversely isotropic medium.

For slate, the transversely isotropic nature of the sample also counts for velocities. Thus, for any localization model a good knowledge on the relation between direction and

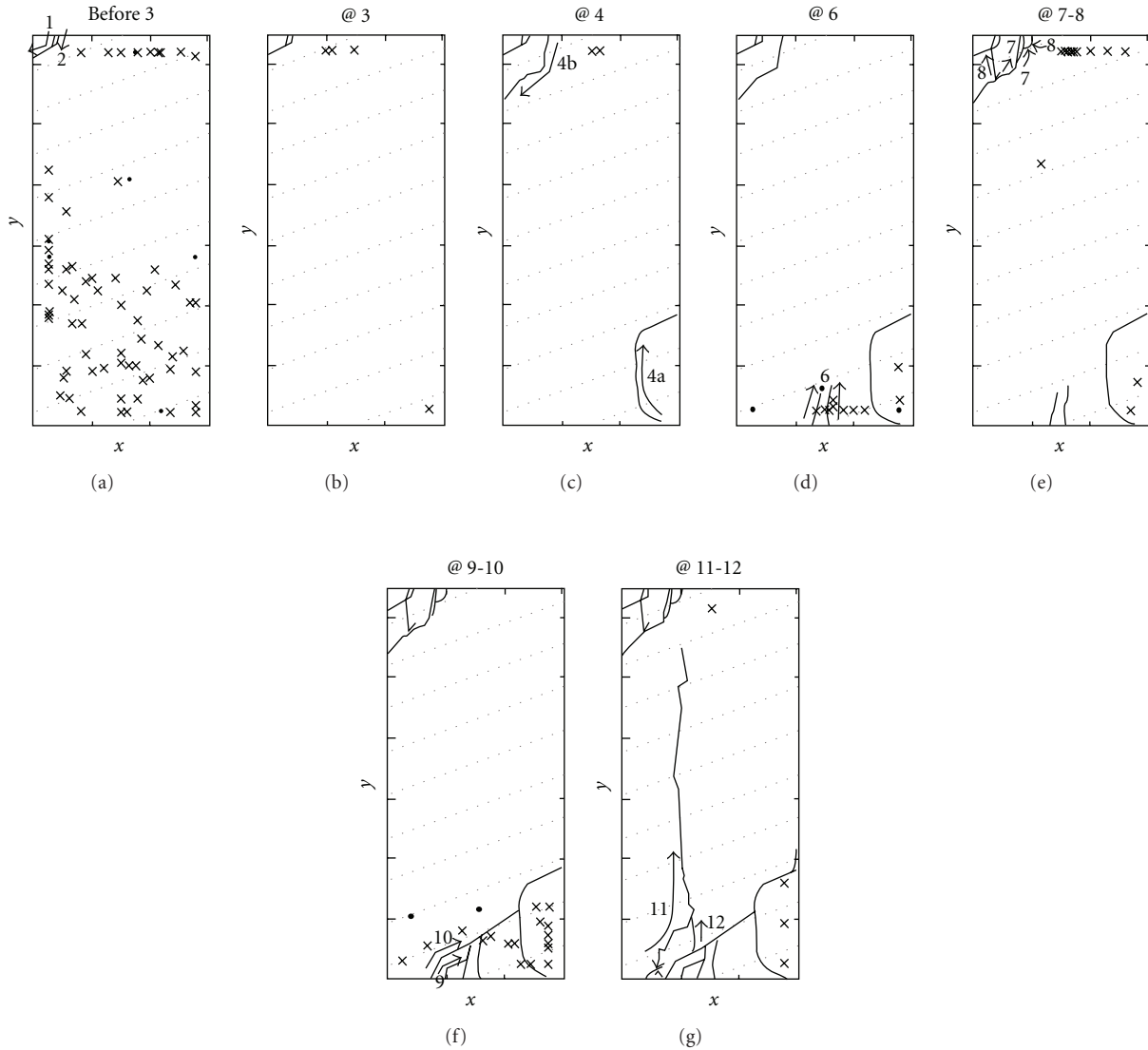


FIGURE 11: Slate sample B02. The occurrence of new fractures during different phases as observed on crosses and dots are hits localized during these phases, respectively, in the back half or in the front half of the sample. Fractures are drawn as they were observed on the front surface of the sample during testing.

velocity is needed, contrary to isotropic media, where the velocity is limited to one value. The technique is validated for 2D by an experimental setup where hits are induced artificially, resulting in good position estimates. The average position error in this test is 3.7 mm and 74% of the points are localized with an error smaller than 4.5 mm (which corresponds to the radius of the applied sensors).

It is observed that for a limited thickness of the sample (30 mm), a 2D approximation gives insufficient results. Hits that arise on the other side of the sample than the sensors need extra travel time to cross the thickness that cannot be neglected when calculating positions. Thus, the velocity anisotropy has to be modelled within three dimensions.

The technique is applied on a series of load tests on slate samples. For most tests, a fair number of hits are localized

during loading. As most hits are found in the back of the sample, it became clear that the load dependence of the velocities should be taken into account. A decrease of postpeak velocity, which agrees to the common theory, distributes the calculated positions more evenly over the thickness of the sample, as one would expect. In addition to this, the positions of the hits during the tests can mostly be correlated roughly with the visual observations of fractures. A more exact positioning demands further study.

The results of these first series of tests are satisfying and insight is gained in factors that can enhance future test results. A larger number of sensors and a more detailed knowledge on load dependence of the velocities can increase the number of localized hits as well as increase the quality of localization.

References

- [1] P. B. Attewell and M. R. Sandford, "Intrinsic shear strength of a brittle, anisotropic rock-I. Experimental and mechanical interpretation," *International Journal of Rock Mechanics and Mining Science & Geomechanics Abstracts*, vol. 11, no. 11, pp. 431–438, 1974.
- [2] M. H. B. Nasser, K. S. Rao, and T. Ramamurthy, "Anisotropic strength and deformation behavior of Himalayan schists," *International Journal of Rock Mechanics and Mining Sciences*, vol. 40, no. 1, pp. 3–23, 2003.
- [3] P. B. Attewell and M. R. Sandford, "Intrinsic shear strength of a brittle, anisotropic rock - III. Textural interpretation of failure," *International Journal of Rock Mechanics and Mining Science & Geomechanics Abstracts*, vol. 11, no. 11, pp. 439–451, 1974.
- [4] C. S. Chen, E. Pan, and B. Amadei, "Fracture mechanics analysis of cracked discs of anisotropic rock using the boundary element method," *International Journal of Rock Mechanics and Mining Sciences & Geomechanics Abstracts*, vol. 35, no. 2, pp. 195–218, 1998.
- [5] B. Debecker and A. Vervoort, "Observation of the fracture process in layered rock by video-imaging," in *Proceedings of the Horizons de l'Optique*, pp. 116–117, 2007.
- [6] B. Debecker, "Experimental observation of fracture patterns in layered slate," *International Journal of Fracture*, vol. 159, no. 1, pp. 51–62, 2009.
- [7] S. V. Lomov, A. Willems, I. Verpoest, Y. Zhu, M. Barbarski, and T. Stoilova, "Picture frame test of woven composite reinforcements with a full-field strain registration," *Textile Research Journal*, vol. 76, no. 3, pp. 243–252, 2006.
- [8] A. Vervoort, M. Wevers, R. Swennen, R. Roels, M. Van Geet, and E. Sellers, "Recent advances of X-ray CT and its applications for rock material," in *X-Ray CT for Geomaterials*, J. Otani and Y. Obara, Eds., pp. 79–91, Swets & Zeitlinger, Lisse, The Netherlands, 2004.
- [9] X. T. Feng, S. Chen, and H. Zhou, "Real-time computerized tomography (CT) experiments on sandstone damage evolution during triaxial compression with chemical corrosion," *International Journal of Rock Mechanics and Mining Sciences*, vol. 41, no. 2, pp. 181–192, 2004.
- [10] A. Tobias, "Acoustic-emission source location in two dimensions by an array of three sensors," *Non-Destructive Testing*, vol. 9, no. 1, pp. 9–12, 1976.
- [11] D. S. Gardiner and L. H. Pearson, "Acoustic emission monitoring of composite damage occurring under static and impact loading," *Journal of Architectural Education*, vol. 4, no. 2, pp. 199–202, 1985.
- [12] C. U. Grosse, H. W. Reinhardt, and F. Finck, "Signal-based acoustic emission techniques in civil engineering," *Journal of Materials in Civil Engineering*, vol. 15, no. 3, pp. 274–279, 2003.
- [13] J.-P. Favre and J.-C. Laizet, "Acoustic emission analysis of the accumulation of cracks in CFRP cross-ply laminates under tensile loading," *Journal of Architectural Education*, vol. 9, no. 2, pp. 97–102, 1990.
- [14] B. Castagnede, W. Sachse, and K. Y. Kim, "Location of pointlike acoustic emission sources in anisotropic plates," *Journal of the Acoustical Society of America*, vol. 86, no. 3, pp. 1161–1171, 1989.
- [15] F. Ciampa and M. Meo, "A new algorithm for acoustic emission localization and flexural group velocity determination in anisotropic structures," *Composites A*, vol. 41, no. 12, pp. 1777–1786, 2010.
- [16] J. J. Scholey, P. D. Wilcox, M. R. Wisnom, and M. I. Friswell, "A practical technique for quantifying the performance of acoustic emission systems on plate-like structures," *Ultrasonics*, vol. 49, no. 6-7, pp. 538–548, 2009.
- [17] T. Kundu, S. Das, S. A. Martin, and K. V. Jata, "Locating point of impact in anisotropic fiber reinforced composite plates," *Ultrasonics*, vol. 48, no. 3, pp. 193–201, 2008.
- [18] S. Aicher, L. Höfflin, and G. Dill-Langer, "Damage evolution and acoustic emission of wood at tension perpendicular to fiber," *Holz als Roh—und Werkstoff*, vol. 59, no. 1-2, pp. 104–116, 2001.
- [19] B. Debecker, *Influence of planar heterogeneities on the fracture behaviour of rock*, Ph.D. thesis, KULeuven, Leuven, Belgium, 2009.
- [20] F. De Barquin and D. Nicaise, "Trial run on Walloon stones in the framework of marking CE 2004-2005," WTCB Report, 2005.
- [21] A. Nielsen, *AE Source Based on Lead Pencil Breaking*, Danish Welding Institute, Svensjecentralen, Copenhagen, 1980.
- [22] B. Van de Steen, *Effect of heterogeneities and defects on the fracture pattern in brittle rock*, Ph.D. thesis, KULeuven, Leuven, Belgium, 2001.
- [23] L. Thomsen, "Weak elastic anisotropy," *Geophysics*, vol. 51, no. 10, pp. 1954–1966, 1986.
- [24] A. Lavrov, A. Vervoort, M. Wevers, and J. A. L. Napier, "Experimental and numerical study of the Kaiser effect in cyclic Brazilian tests with disk rotation," *International Journal of Rock Mechanics and Mining Sciences*, vol. 39, no. 3, pp. 287–302, 2003.
- [25] J. F. Labuz, H. S. Chang, C. H. Dowding, and S. P. Shah, "Parametric study of acoustic emission location using only four sensors," *Rock Mechanics and Rock Engineering*, vol. 21, no. 2, pp. 139–148, 1988.
- [26] T. E. Unander, *Acoustic emission measurements in petroleum-related rock mechanics*, Ph.D. thesis, NTNU, Trondheim, Norway, 2002.
- [27] I. G. Scott, "Basic acoustic emission," in *Nondestructive Testing and Monographs and Tracts*, W. J. McGonagle, Ed., vol. 6, p. 69, Gordon and Breach Science Publishers, New York, NY, USA, 1991.
- [28] J. F. Couvreur, A. Vervoort, M. S. King, E. Lousberg, and J. F. Thimus, "Successive cracking steps of a limestone highlighted by ultrasonic wWave propagation," *Geophysical Prospecting*, vol. 49, pp. 71–78, 2001.
- [29] M. R. Ayling, P. G. Meredith, and S. A. F. Murrell, "Micro-cracking during triaxial deformation of porous rocks monitored by changes in rock physical properties, I. Elastic-wave propagation measurements on dry rocks," *Tectonophysics*, vol. 245, no. 3-4, pp. 205–221, 1995.



Hindawi

Submit your manuscripts at
<http://www.hindawi.com>

